Investigation of Input-Output Waveform Engineered Continuous Inverse Class F Power Amplifiers

Sagar K. Dhar, Tushar Sharma, *Student Member, IEEE,* Ramzi Darraji, Damon G. Holmes, *Member, IEEE,* Suhas V. Illath, Vince Mallette, and Fadhel M. Ghannouchi, *Fellow, IEEE*

***Abstract*— An in-depth analysis of the continuous inverse Class F power amplifier (PA) accounting for nonlinear input and output active device properties is presented. The analyses show possible ways of exploiting input nonlinearity to improve and maintain PA performance in a broadband operation and propose a flexible source second harmonic design space which reduces the input matching network (MN) design complexities. Such exploitation of input nonlinearity can also alleviate performance degradation due to dynamic knee behaviour of a practical field effect transistor (FET) in continuous inverse Class F PA operation. The analyses are validated with vector load pull (VLP) measurements and utilized to implement a broadband PA design. High drain efficiency over 75% and output power more than 38 dBm are achieved over 0.8-1.4 GHz at constant 3 dB gain compression.**

***Index Terms*—continuous mode PA, harmonic tuned PA, input harmonics, inverse class F, multi-harmonic load pull, RF power amplifier, pulsed wave load pull, waveform engineering.**

I. Introduction

HIGH EFFICIENCY power amplifier (PA) is an integral part of efficient radio frequency (RF) transmitting system design. To enable modern and future wireless communication system, the quest for efficient, wideband, and linear PA design techniques is ongoing. Pushed by such high interest, the efficient PA design techniques are shifted from the tuned load (TL) to harmonic tuned (HT) strategies [1] leaving the job of improving linearity by digital signal processing. In the HT PAs [2]–[9], load harmonic voltage and current components are utilized to shape the drain voltage and current waveforms such that their overlapping is reduced, and device power dissipation is decreased. This is typically realized by terminating the second and third harmonic loads at either short or open (e.g. Class F, inverse Class F). Although such constraints in harmonic termination increase the matching network (MN) realization complexity they ensure an increase in PA efficiency performance [10]. Nevertheless, these design approaches are mainly for single frequency applications due to the constraints of single and fixed harmonic terminations. To overcome this and to realize wideband operation, continuous mode PA design techniques have been proposed [11]–[29]. In the continuous mode of PA operation, load harmonic terminations are swept near open or short which allows flexibility in output matching network (MN) design and realization for wideband operation and maintains PA performance over the band.

The above-mentioned works consider input source harmonic to be short circuited. Such consideration is under the fact that the impact of source harmonic terminations other than short circuit generates input nonlinearity at the intrinsic gate node and can be detrimental to PA performance [30], [31]. Thus, the input nonlinearity of the active device is avoided either by short circuit termination [32], [33] or by counteracting nonlinearity [34]. In practice, the source harmonics are designed near short to allow flexibility in MN design, but, the potential of input nonlinearity and its impact on waveform shaping has not been fully explored nor analyzed for continuous-mode HT PAs. Although, the impact of input nonlinearity is investigated in [35]–[37], a complete analysis and explanation is still missing for continuous-mode HT PAs.

In this work, a comprehensive theoretical analysis of input and output waveform engineered continuous-mode inverse Class F PA is presented. This paper expands on the related conference paper [38], which demonstrated the performance degradation of output-engineered continuous-mode inverse class F PAs due to variable knee voltage effect. Here, we present more generic analysis under input nonlinearity (both magnitude and phase) and perform a detailed investigation of the dynamic knee voltage behaviour of continuous-mode inverse class PAs in the presence of input nonlinearity.

A functional block diagram of the PA is shown in Fig. 1. In this paper, we leverage the combined benefits of input and

This paper is an expanded version from the IEEE Latin America Microwave Conference 2018, Arequipa, Peru, December 12-14, 2018.

S. K. Dhar, and F. M. Ghannouchi are with the University of Calgary, Calgary, AB T2N 1N4, Canada. (e-mail: sagar.dhar@ucalgary.ca; fadhel.ghannouchi@ucalgary.ca).

T. Sharma is with the Department of Electrical and Computer Engineering, Princeton University, USA, and was with the NXP Semiconductors, Chandler, AZ 85224, USA. (e-mail: tsharm@princeton.edu).

R. Darraji is with the Ericsson Canada Inc. Ottawa, ON K2K 2V6, Canada. (email: ramzi.darraji@ericsson.com)

D. G. Holmes is with the NXP Semiconductors, Chandler, AZ 85224 USA (e-mail: damon.holmes@nxp.com).

S. V. Illath, and V. Mallette are with the Focus Microwaves, Quebec, Canada. (email: suhas@focus-microwaves.com; vince@focus-microwaves.com).

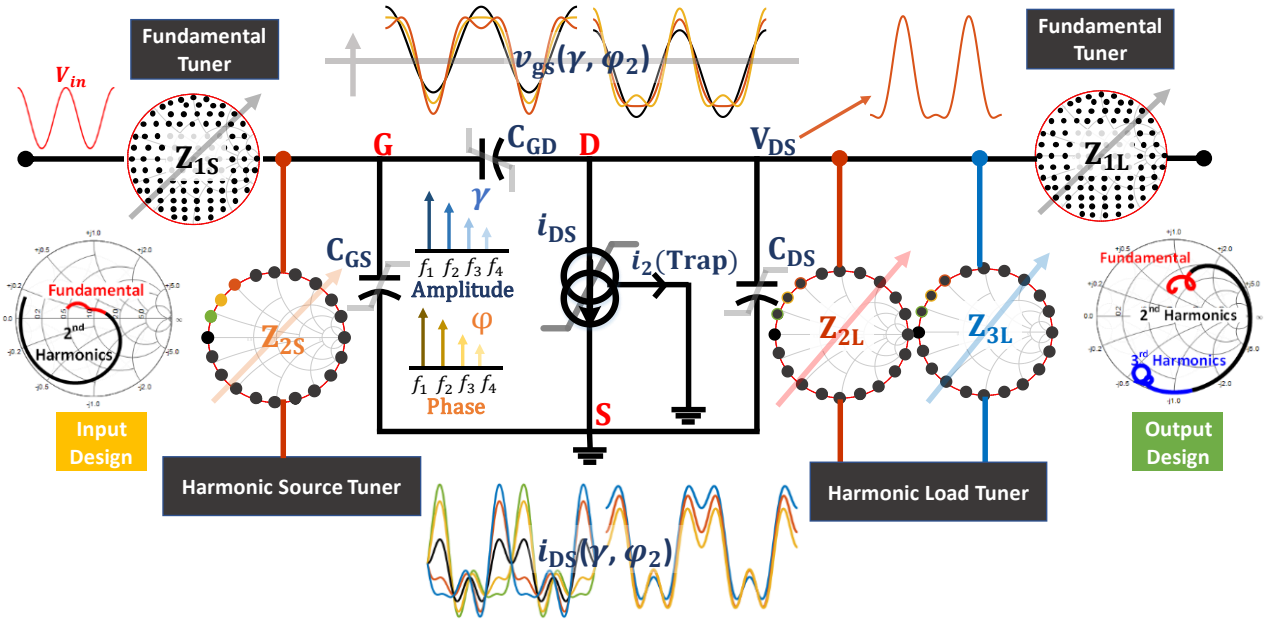

Fig. 1. Functional block diagram of an inverse Class F PA with input nonlinearity.

output harmonic manipulation and develop a continuous-mode inverse Class F PA with high efficiency over a wide frequency range. A primary contribution of this work is in demonstrating that input harmonic tuning can help to alleviate the problem of variable knee voltage behaviour of typical continuous-mode inverse Class F PAs. Additionally, we demonstrate that input nonlinearity influences the drain current waveforms, consequently, the load design space. Following the analysis and load pull validation, a wideband PA is designed and implemented covering 0.8-1.4 GHz with small signal gain more than 12 dB, efficiency over 75%, and output power more than 38 dBm at constant 3 dB gain compression.

The remainder of this paper is organized as follows. In Section II, the generalized theory of inverse Class F PA and its continuous mode of operation with input and output nonlinearity is presented. The load pull validation of the theory is presented in Section III. In Section IV, PA implementation and measurement results are reported.

II. Input-Output Waveform Engineering Theory

The gate voltage and drain current waveforms of a tuned load PA under Class B bias condition can be expressed as [1]

$$v_{GS,B}(\theta) = V_{GS0} + V_1 \cos\theta \tag{1}$$

$$i_{DS,B}(\theta) = \begin{cases} I_{max}\cos\theta, & -\frac{\pi}{2} \le \theta \le \frac{\pi}{2} \\ 0, & -\pi \le \theta \le -\frac{\pi}{2}, \frac{\pi}{2} \le \theta \le \pi \end{cases} \tag{2}$$

$$i_{DS,B}(\theta) = I_{DC,B} + \sum_{n=1}^{\infty} I_n \cos(n\theta)$$

where V_{GS0} is the gate bias voltage, V_1 is the fundamental gate voltage component, I_{max} is the maximum current limit of the device, and $I_{DC,B}$, I_n denoting the DC and Fourier current components, respectively. The harmonic terminations for both input and output are considered short in (1) and (2). With second harmonic input non-linearity at the gate node, the voltage waveform can be expressed and normalized as

$$v_{GS}(\theta) = V_{GS0} + V_1 \cos\theta + V_2 \cos(2\theta + \varphi_2) \tag{3}$$

$$v_{GS,\text{norm}}(\theta, \gamma, \varphi_2) = \frac{v_{GS}(\theta) - V_{GS0}}{V_1} = \cos\theta + \gamma\cos(2\theta + \varphi_2) \tag{4}$$

where V_2 is the second harmonic gate voltage component, φ_2 is the phase difference between fundamental and second harmonic voltage component and $\gamma = V_2 / V_1$ is defined as the input nonlinearity factor. The gate voltage waveforms for different input nonlinearity factor, γ, and phase difference, φ_2, are shown in Fig. 2(a-d). Based on the γ and φ_2, the gate voltage waveforms are shaped and consequently, alters the drain current waveforms. The drain current waveform can be deduced considering a constant trans-conductance device for a Class B bias condition as

$$i_{DS}(\theta, \gamma, \varphi_2) = \begin{cases} I_{max}[\cos\theta + \gamma\cos(2\theta + \varphi_2)], & -\frac{\beta}{2} \le \theta \le \frac{\beta}{2} \\ 0, & -\pi \le \theta \le -\frac{\beta}{2}, \frac{\beta}{2} \le \theta \le \pi \end{cases} \tag{5}$$

$$i_{DS}(\theta, \gamma, \varphi_2) = I_{DC} + \sum_{n=1}^{\infty} I_{nr}\cos(n\theta) + \sum_{n=1}^{\infty} I_{nq}\sin(n\theta)$$

where, β is the modified conduction angle by gate voltage waveform shaping due to second order input nonlinearity, I_{DC} is the DC drain current component, and I_{nr}, I_{nq} is the Fourier drain current components of real and reactive components of $i_{DS}(\theta)$, respectively. The effective conduction angle due to input waveform shaping can be deduced by setting $i_{DS}(\theta) = 0$ and can be related to γ and φ_2 as

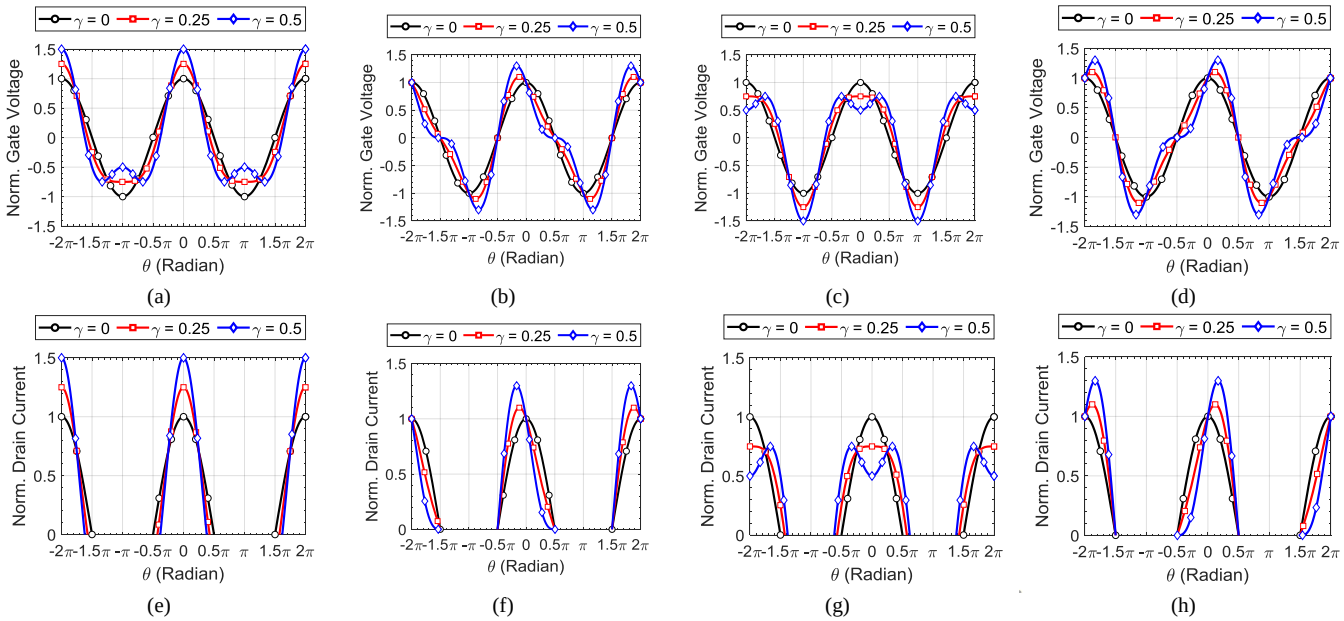

Fig. 2. Gate voltage: (a) $\varphi_2 = 0$, (b) $\varphi_2 = \pi/2$, (c) $\varphi_2 = \pi$, (d) $\varphi_2 = 3\pi/2$, and drain current: (e) $\varphi_2 = 0$, (f) $\varphi_2 = \pi/2$, (g) $\varphi_2 = \pi$, (h) $\varphi_2 = 3\pi/2$ waveforms with second harmonic input nonlinearity for a Class B bias.

$$\cos\frac{\beta}{2} + \gamma\cos(\beta + \varphi_2) = 0 \tag{6}$$

The variation of the conduction angle of the device under the presence of input nonlinearity is shown in Fig. 3(a) for a Class B bias condition. The conduction angle changes widely due to input nonlinearity from ~130° to ~230° compared to the original conduction angle of 180°. Although, the conduction angle is reported to be increased by input nonlinearity (where the phase difference φ_2 is considered to be 180°) in previous works [30], [39] and thus detrimental to PA efficiency, this analysis shows that the conduction angle depends on the phase difference between input fundamental and harmonic voltage components. Thus, the previous works can be considered as special cases of this work. The resultant current waveforms for different γ and φ_2 are illustrated in Fig. 2(e-h) for Class B bias condition. It is worth mentioning here that the input non-linearity results in not only a wide variation in conduction angle, but also changes the shape of the current waveform from its original shape of half sinusoidal for a TL PA with Class B bias condition. Due to the presence of input non-linearity, current peaking, as well as the asymmetry of the drain current with respect to Y-axis, occurs which results in quadrature current components in (5). The variation of efficiency of a Class B PA with input nonlinearity is calculated and shown in Fig. 3(b). The input nonlinearity significantly impacts the efficiency performance of a Class B PA. While an optimum combination of γ and φ_2 can result in maximum efficiency of 88%, it can be degraded to the lowest value of 50% if the worst combination of γ and φ_2 is considered. When $\gamma = 0$, the efficiency in Fig. 3(b) converges to the conventional Class B PA with input and output harmonic terminations as short-circuited and shows the efficiency of 78.5%. This ensures the accuracy of the theoretical calculation.

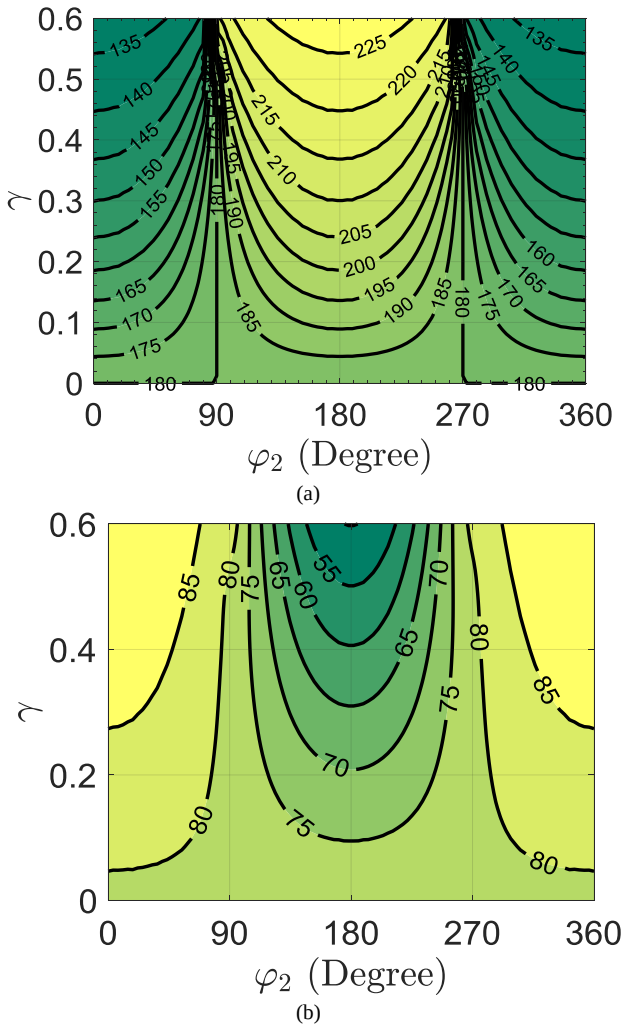

Fig. 3. (a) Variation of conduction angle, and (b) variation of efficiency with input nonlinearity of a Class B PA.

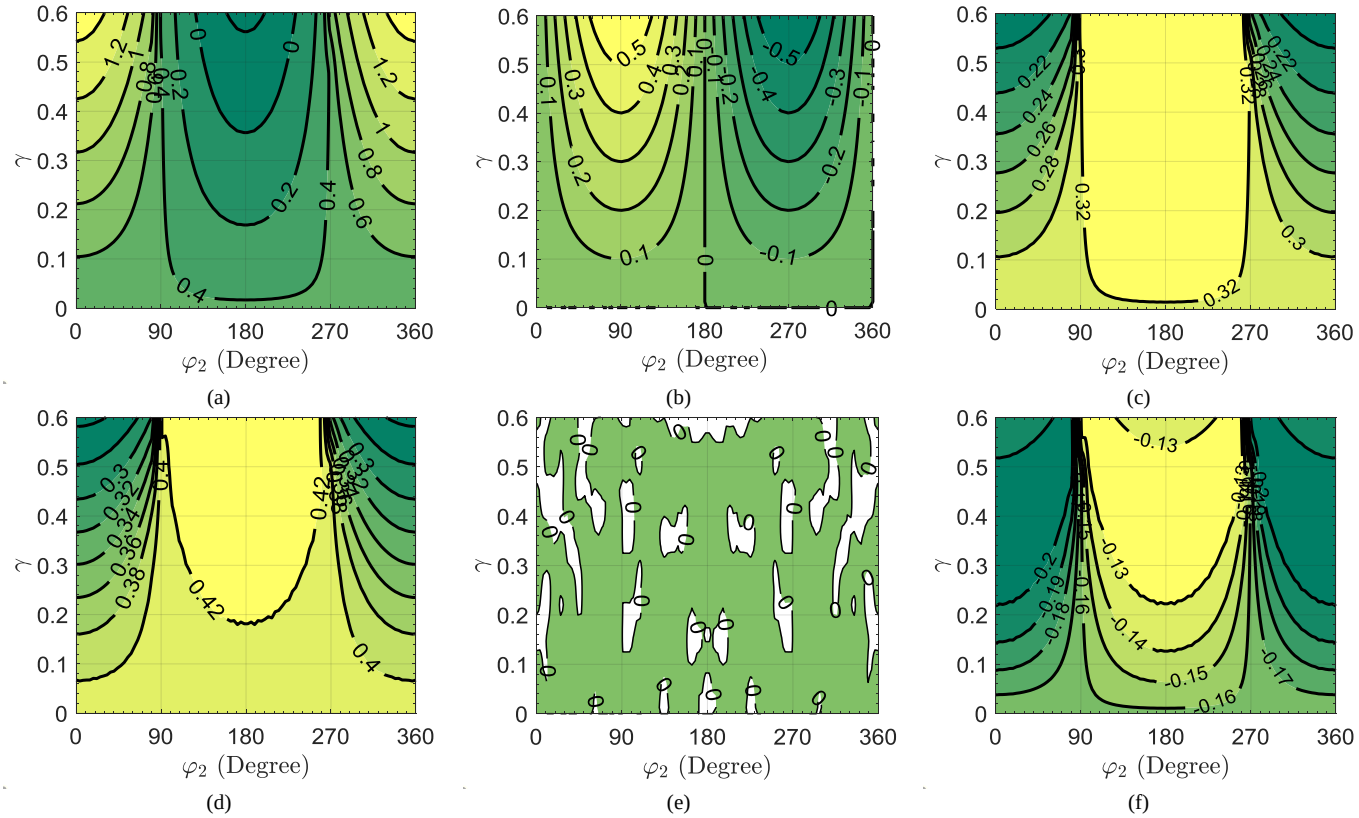

Fig. 4. Variation with input nonlinearity in terms of input nonlinearity factor, γ, and phase difference, φ_2 of (a) normalized χ, real coefficient of i_2, (b) normalized ξ, reactive coefficient of i_2, (c) normalized I_{DC}, DC current component of $i_{DS,F^{-1}}$, (d) normalized I_{1r}, fundamental real current component of $i_{DS,F^{-1}}$, (e) normalized I_{2r}, second harmonic real current component of $i_{DS,F^{-1}}$, (f) normalized I_{3r}, third harmonic real current component of $i_{DS,F^{-1}}$.

A. *Input-Output Engineered Inverse Class F PA Analysis*

For an inverse Class F PA, the second harmonic load is terminated as an open circuit at the intrinsic drain node. Although the active device generates the second harmonic drain current, it cannot be sustained due to an open circuit termination. Thus, the intrinsic drain current waveform of an inverse Class F PA is derived modifying (5) using current trapping technique as

$$i_{DS,F^{-1}}(\theta,\gamma,\varphi_2)=\begin{cases}\mathrm{I}_{\max}[\cos\theta+\gamma\cos(2\theta+\varphi_2)]-\\ \left(\chi\cos 2\theta-\xi\sin 2\theta\right),\ -\dfrac{\beta}{2}\le\theta\le\dfrac{\beta}{2}\\ 0,\ -\pi\le\theta\le-\dfrac{\beta}{2},\dfrac{\beta}{2}\le\theta\le\pi\end{cases} \quad (7)$$

$$i_{DS,F^{-1}}(\theta,\gamma,\varphi_2)=I_{DC}+\sum_{n=1}^{\infty}I_{nr}\cos(\mathrm{n}\,\theta)+\sum_{n=1}^{\infty}I_{nq}\sin(\mathrm{n}\,\theta)$$

where, $i_2=\chi\cos 2\theta-\xi\sin 2\theta$, and χ, ξ denote the coefficients for real and reactive terms of second harmonic drain current, respectively. The exclusion of second harmonic drain current components impacts the shape as well as the peak of the drain current waveform. The coefficients χ and ξ can be computed as a function of β, γ, and φ_2 by equating the real (I_{2r}) and imaginary (I_{2q}) part of the second harmonic current to zero as

$$I_{2r}=\frac{1}{\pi}\int_{-\beta/2}^{+\beta/2}i_{DS,F^{-1}}(\theta).\cos 2\theta\ d\theta=0 \quad (8)$$

$$I_{2q}=\frac{1}{\pi}\int_{-\beta/2}^{+\beta/2}i_{DS,F^{-1}}(\theta).\sin 2\theta\ d\theta=0 \quad (9)$$

From (6)-(9), χ and ξ are calculated as functions of β, γ, and φ_2 as

$$\chi(\beta,\gamma,\varphi_2)=\mathrm{I}_{max}\frac{3\gamma\cos\varphi_2(2\beta+\sin 2\beta)-16\sin^3\frac{\beta}{2}+24\sin\frac{\beta}{2}}{6\beta+3\sin 2\beta} \quad (10)$$

$$\xi(\gamma,\varphi_2)=\gamma\,\mathrm{I}_{max}\sin\varphi_2 \quad (11)$$

It is no surprise that the coefficient of reactive term, ξ, is not zero unlike inverse Class F amplifier with second harmonic source impedance short-circuited, but a function of γ, and φ_2 which appears due to the input second harmonic nonlinearity. The dc (I_{DC}), fundamental (I_{1r}), second harmonic (I_{2r}) and third harmonic (I_{3r}) components of drain current ($i_{DS,F^{-1}}$,) can be calculated as functions β, γ, and φ_2 as

$$I_{DC}(\beta,\gamma,\varphi_2)=\frac{1}{2\pi}\left(2\,\mathrm{I}_{max}\sin\frac{\beta}{2}-\left(\chi-\gamma\,\mathrm{I}_{max}\cos\varphi_2\right)\sin\beta\right) \quad (12)$$

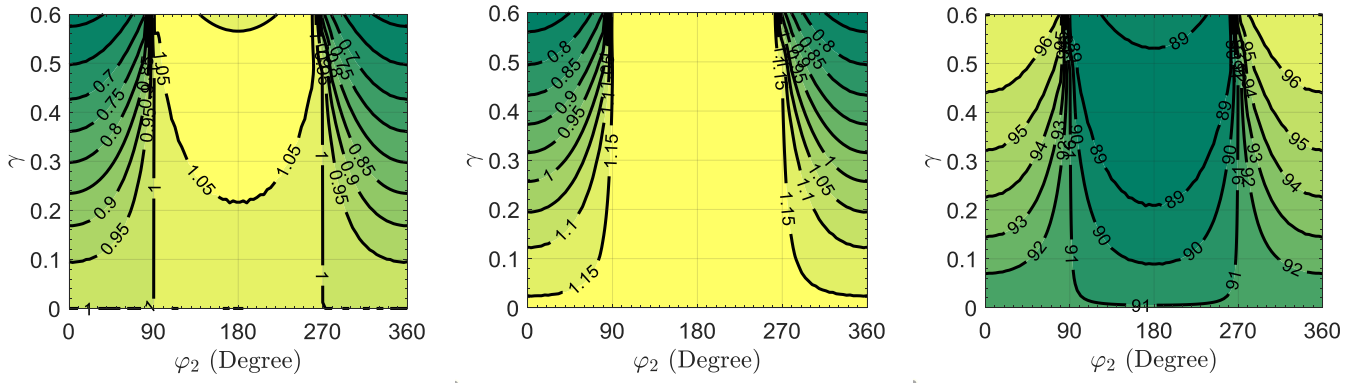

(a) (b) (c)

Fig. 6. Variation of (a) normalized DC power, (b) normalized output power, and (c) efficiency with input nonlinearity factor, γ, and phase difference, φ_2, when device knee voltage, $V_K = 0$.

$$I_{1r}(\beta,\gamma,\varphi_2)=\frac{I_{max}}{2\pi}(\beta+\sin\beta)-\frac{\chi}{\pi}\left(\sin\frac{\beta}{2}+\frac{1}{3}\sin\frac{3\beta}{2}\right)+\frac{\gamma I_{max}\cos\varphi_2}{3\pi}\left(3\sin\frac{\beta}{2}+\sin\frac{3\beta}{2}\right) \quad (13)$$

$$I_{1q}(\beta,\gamma,\varphi_2)=\frac{1}{3\pi}\left[4\xi\sin^3\frac{\beta}{2}-\gamma I_{max}\sin\varphi_2\left(3\sin\frac{\beta}{2}-\sin\frac{3\beta}{2}\right)\right] \quad (14)$$

$$I_{2r}(\beta,\gamma,\varphi_2)=\frac{I_{max}}{\pi}\left(2\sin\frac{\beta}{2}-\frac{4}{3}\sin^3\frac{\beta}{2}\right)-\frac{(\chi-\gamma I_{max}\cos\varphi_2)}{\pi}\left(\frac{\beta}{2}+\frac{1}{4}\sin 2\beta\right) \quad (15)$$

$$I_{2q}(\beta,\gamma,\varphi_2)=\frac{1}{4\pi}\left[(\xi-\gamma I_{max}\sin\varphi_2)(2\beta-\sin 2\beta)\right] \quad (16)$$

$$I_{3r}(\beta,\gamma,\varphi_2)=\frac{I_{max}\sin\beta}{2\pi}(1+\cos\beta)-\frac{(\chi-\gamma I_{max}\cos\varphi_2)}{\pi}\left(\sin\frac{\beta}{2}+\frac{1}{5}\sin\frac{5\beta}{2}\right) \quad (17)$$

$$I_{3q}(\beta,\gamma,\varphi_2)=\frac{1}{\pi}\left[(\xi-\gamma I_{max}\sin\varphi_2)\left(\sin\frac{\beta}{2}-\frac{1}{5}\sin\frac{5\beta}{2}\right)\right] \quad (18)$$

For the higher order harmonic current components, $n > 3$, the coefficients can be calculated as

$$I_{nr}(\beta,\gamma,\varphi_2)=\frac{1}{\pi}I_{max}\left(\frac{1}{n-1}\sin\frac{(n-1)\beta}{2}+\frac{1}{n+1}\sin\frac{(n+1)\beta}{2}\right)-\frac{\chi}{\pi}\left(\frac{1}{n-2}\sin\frac{(n-2)\beta}{2}+\frac{1}{n+2}\sin\frac{(n+2)\beta}{2}\right)-\frac{2\gamma I_{max}\cos\varphi_2}{\pi(n^2-4)}\left(\sin\beta\cos\frac{n\beta}{2}-\sin\frac{(n-2)\beta}{2}\right) \quad (19)$$

$$I_{nq}(\beta,\gamma,\varphi_2)=\frac{\xi}{\pi}\left(\frac{1}{n-2}\sin\frac{(n-2)\beta}{2}-\frac{1}{n+2}\sin\frac{(n+2)\beta}{2}\right)-\frac{2\gamma I_{max}\sin\varphi_2}{\pi(n^2-4)}\left(2\cos\beta\sin\frac{n\beta}{2}-n\sin\beta\cos\frac{n\beta}{2}\right) \quad (20)$$

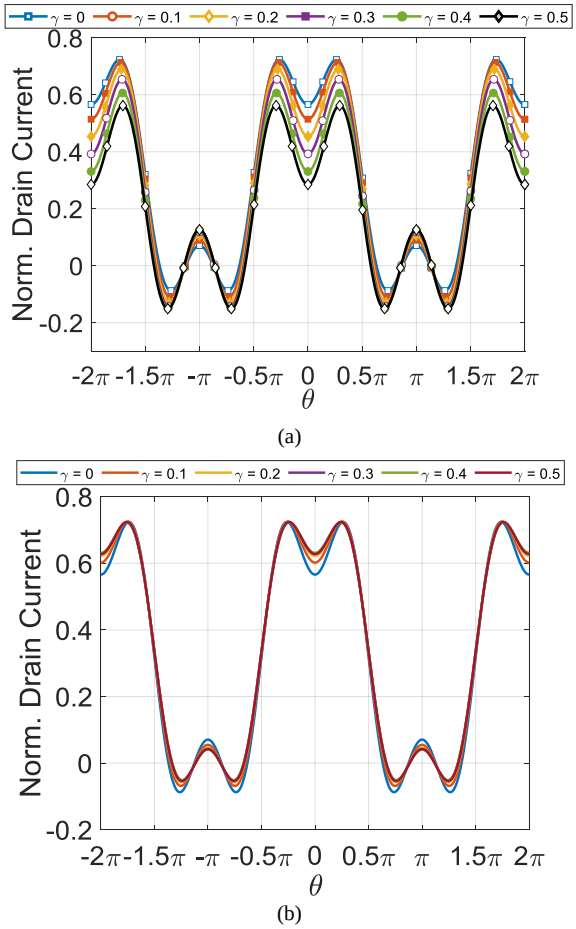

(a)

(b)

Fig. 5. Drain current waveforms for different nonlinearity factor: (a) at $\varphi_2 = 0$, and (b) at $\varphi_2 = \pi$.

Due to the input nonlinearity, second harmonic drain current component is generated by the active device. However, that contribution is reduced out by the second harmonic open circuit loading condition for inverse Class F mode of operation. The variations of cancelling factors, χ and ξ, with input nonlinearity are shown in Fig. 4(a) and Fig. 4(b). The variation of χ and ξ is such that the second harmonic drain current components, I_{2r} and I_{2q}, are zero for inverse Class F mode of operation as shown in Fig. 4(e). Since, the DC, fundamental, and third harmonic

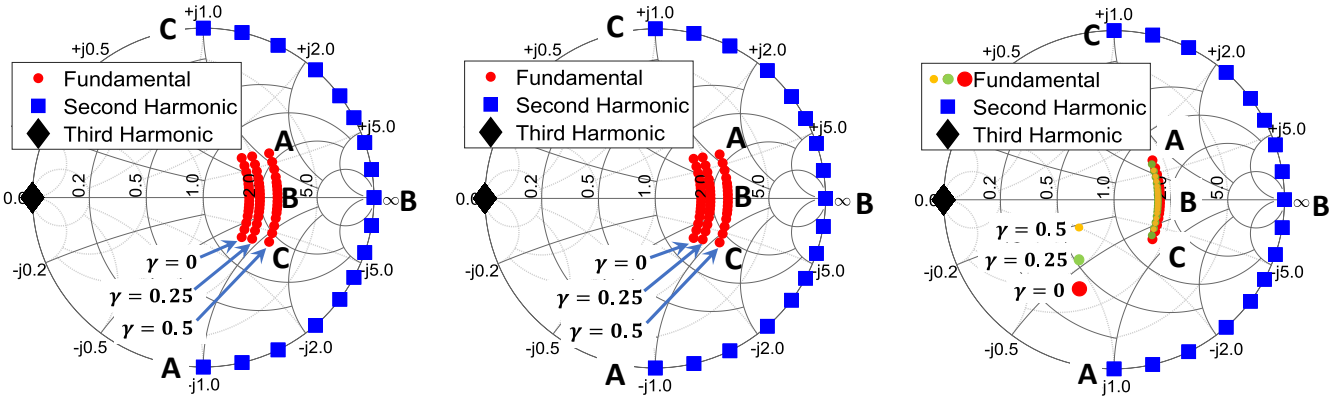

Fig. 7. Intrinsic load design space variation with input nonlinearity of a continuous inverse Class F PA at (a) $\varphi_2 = 0$, (b) $\varphi_2 = \pi/3$, and (c) $\varphi_2 = \pi$.

Fourier coefficients are dependent on χ and ξ, the input nonlinearity also impacts their values. The variation is illustrated in Fig. 4(c), 4(d) and 4(f). By using up to first three harmonic components, the drain current can be reconstructed and shown in Fig. 5 for different input nonlinearity factor. At $\varphi_2 = 0$, drain current waveform varies significantly as shown in Fig. 5(a) due to the variation of Fourier coefficients (especially, I_{DC} and I_{1r}) at different levels of γ. A similar trend is expected in the range of $0 < \varphi_2 < 90°$ and $270° < \varphi_2 < 360°$. On the other hand, the coefficients are almost constant when γ changes at $\varphi_2 = \pi$, thus, the drain current waveforms are almost similar as shown in Fig. 5(b). Same is true in the range of $90° < \varphi_2 < 270°$. It is worth mentioning here that the exclusion of second harmonic drain current by trapping technique also cancels out the asymmetric drain current characteristics (shown in Fig. 2) introduced by input non-linearity and make the drain current waveform symmetric with respect to Y-axis as can be seen from Fig. 5. This consequently causes reactive Fourier current coefficients (I_{nq}) of $i_{DS,F^{-1}}$ to be zero.

To compute output power and efficiency, the drain voltage of inverse Class F PA is considered as [1]

$$v_{DS,F^{-1}}(\theta) = V_{DD} - \sqrt{2}(V_{DD} - V_K)\left(\cos\theta - \frac{1}{2\sqrt{2}}\cos 2\theta\right) \quad (21)$$

where V_{DD} and V_K are the drain supply and device knee voltage. Thus, the DC power, output power and drain efficiency can be calculated as

$$P_{DC}(\beta,\gamma,\varphi_2) = V_{DD} \times I_{DC}(\beta,\gamma,\varphi_2) \quad (22)$$

$$P_{OUT}(\beta,\gamma,\varphi_2) = \frac{1}{2} \times \sqrt{2}(V_{DD} - V_K) \times I_{1r}(\beta,\gamma,\varphi_2) \quad (23)$$

$$\eta(\beta,\gamma,\varphi_2) = \frac{\frac{1}{2} \times \sqrt{2}(V_{DD} - V_K) \times I_{1r}(\beta,\gamma,\varphi_2)}{V_{DD} \times I_{DC}(\beta,\gamma,\varphi_2)} \quad (24)$$

The variation of normalized DC power, normalized output power (with respect to Class B DC power and output power), and drain efficiency are presented in Fig. 6. As can be seen from Fig. 6(c), the efficiency of an inverse class F PA varies from 89% to 97% due to input nonlinearity. Also, the efficiency results converge to theoretical 91% efficiency of an inverse Class F PA without input nonlinearity at $\gamma = 0$. Compared to Class B PA, the efficiency remains almost constant. Further, this analysis opens the scope of wide range of input second harmonic terminations possible instead of constant short circuit as in conventional design which is valuable in wideband PA design techniques.

B. Continuous Inverse Class F PA Analysis

For continuous-mode of inverse class F operation, the second harmonic load impedance is swept near open on the edge of the Smith chart. Thus, the second harmonic load termination can be defined as

$$Z_{2L} = -\frac{V_{2r} - jV_{2q}}{I_{2r} - jI_{2q}} = jX_2 \quad (25)$$

where, V_{2r} and V_{2q} are the real and reactive components of the drain voltage defined in (21), respectively, and X_2 is the second harmonic load reactance of the device. Such reactive termination at second harmonic load will allow the generation of a reactive second harmonic drain current component, I_{2q}. From (14) and (16), I_{1q} and I_{2q} can be related as

$$I_{1q} = I_{2q} \cdot \frac{16}{3} \cdot \frac{\sin^3\frac{\beta}{2}}{2\beta - \sin 2\beta} \quad (26)$$

From (25) and (26), I_{1q} and I_{2q} are defined as functions of X_2 as

$$I_{1q} = -\frac{8}{3} \cdot \frac{V_{DD} - V_K}{X_2} \cdot \frac{\sin^3\frac{\beta}{2}}{2\beta - \sin 2\beta} \quad (27)$$

$$I_{2q} = -\frac{1}{2} \cdot \frac{V_{DD} - V_K}{X_2} \quad (28)$$

Thus, the intrinsic fundamental impedance for continuous inverse Class F PA operation as a function of second harmonic reactance, X_2, can be expressed as

$$Z_{1L} = -\frac{V_{1r} - jV_{1q}}{I_{1r} - jI_{1q}} = \frac{1}{Y_{1L}} \quad (29)$$

where,

$$Y_{1L} = \frac{I_{max}}{\sqrt{2}\pi(V_{DD} - V_K)}\sigma + j\frac{8\sin^3(\beta/2)}{3\sqrt{2}X_2(2\beta - \sin 2\beta)} \quad (30)$$

and,

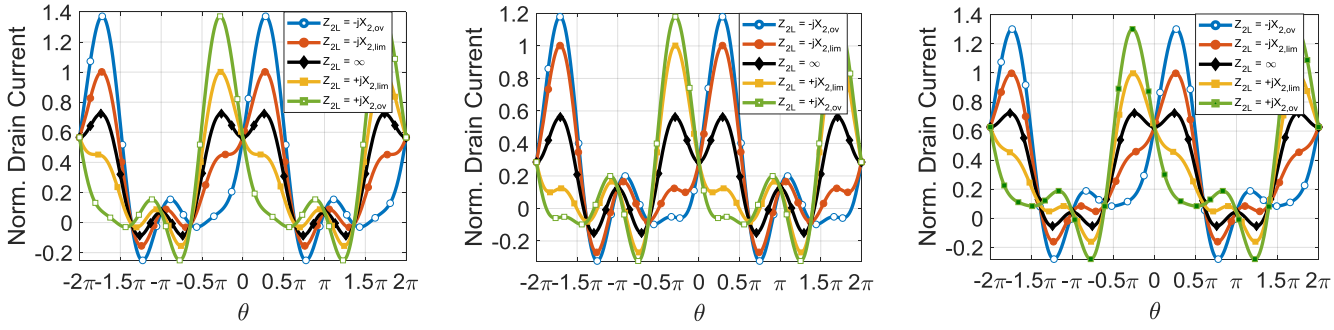

(a) (b) (c)

Fig. 8. Drain current waveforms for continuous mode inverse Class F PA at (a) $\gamma = 0$, $\varphi_2 = 0$, (b) $\gamma = 0.5$, $\varphi_2 = 0$, and (c) $\gamma = 0.5$, $\varphi_2 = \pi$.

$$\sigma = \left(\frac{\beta}{2} + \frac{\sin\beta}{2}\right) - \frac{1}{6\beta + 3\sin 2\beta}.\left(\sin\frac{\beta}{2} + \frac{1}{3}\sin\frac{3\beta}{2}\right).$$
$$\left(24\sin\frac{\beta}{2} - 16\sin^3\frac{\beta}{2} + 3\gamma\cos\varphi_2(2\beta + \sin 2\beta)\right) + \quad (31)$$
$$\frac{1}{3}\gamma\cos\varphi_2\left(3\sin\frac{\beta}{2} + \sin\frac{3\beta}{2}\right)$$

From (29), a set of load design space for continuous inverse Class F operation can be found at different values of γ and φ_2. For example, the design spaces for three different values of γ at $\varphi_2 = 0$, $\pi/3$, and π are shown in Fig. 7 where the third harmonic load termination, Z_{3L}, is short-circuited. A typical trend can be observed that the fundamental load impedance is increased with a higher value of γ (when $\varphi_2 < \pi/2$) which can be explained by the decreased amount of fundamental current component as shown in Fig. 4(d). Thus, the difference/separation of fundamental load design space at different φ_2 values is different based on the level of current component variation.

The resulting drain current waveforms for sweeping Z_{2L} near open on the edge of the Smith chart are shown in Fig. 8. Since, sweeping Z_{2L} results in drain current peaking and might exceed the device maximum limit, I_{max}, (as shown in Fig. 8 for $Z_{2L} = \pm jX_{2,ov}$), it is important to find the maximum limit of X_2. To simplify the computation without loss of generality, the impact of X_2 variation is considered mainly on I_{1q} and I_{2q} (ignoring I_{3q} and higher order harmonics), and the drain current is written as

$$i_{DS,cont}(\theta) = I_{DC} + I_{1r}\cos\theta + I_{1q}\sin\theta + I_{2q}\sin 2\theta + I_{3r}\cos 3\theta \quad (32)$$

Since, the current peak does not occur at $\theta = 0$, the angle of maximum device current, θ_{max}, is found by equating the first derivative to zero and by confirming the second derivative at θ_{max} to be less than zero as

$$i'_{DS,cont}(\theta) = 0 \quad (33a)$$

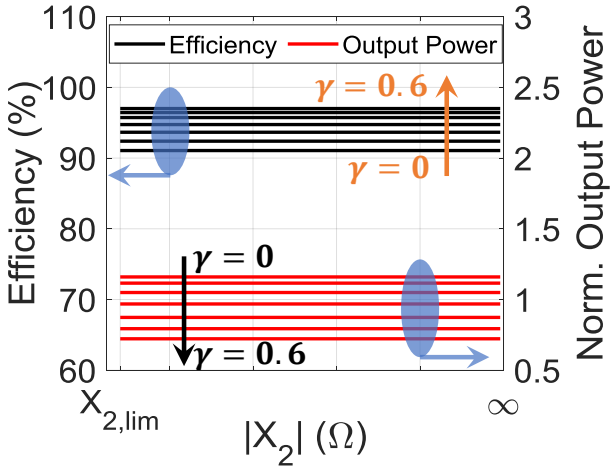

(a)

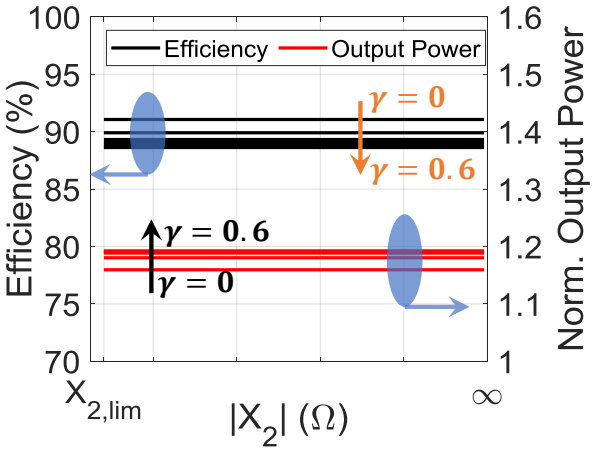

(b)

Fig. 9. Efficiency and output power variation in continuous mode of operation at $\varphi_2 = 0$ (a), and $\varphi_2 = \pi$ (b).

$$\theta_{max} = \pm\cos^{-1}\left(\frac{\sqrt{852\cos\left(\frac{\beta}{2}\right)^2 - 1044\cos\left(\frac{\beta}{2}\right)^4 + 400\cos\left(\frac{\beta}{2}\right)^6 + 144\cos\left(\frac{\beta}{2}\right)^8 - 45\beta^2 + 360\beta\cos\left(\frac{\beta}{2}\right)^3\sin\left(\frac{\beta}{2}\right) - 352}}{4\left(4\cos\left(\frac{\beta}{2}\right)^8 + 10\cos\left(\frac{\beta}{2}\right)^6 - 14\cos\left(\frac{\beta}{2}\right)^4 + 15\beta\sin\left(\frac{\beta}{2}\right)\cos\left(\frac{\beta}{2}\right)^3 + 12\cos\left(\frac{\beta}{2}\right)^2 - 12\right)}}{6}\right) \quad (34)$$

$$i''_{DS,\mathrm{cont}}(\theta_{\max}) < 0 \tag{33b}$$

where, $i'_{DS,cont}$ and $i''_{DS,cont}$ denote the first and second derivative of $i_{DS,cont}$, respectively. The peak angle, θ_{max}, is found as in (34) where γ and φ_2 are replaced as a function of β. For $\gamma = 0$ and $\varphi_2 = 0$ (results in $\beta = \pi$), the peak angle is calculated as

$$\theta_{\max} = \pm\cos^{-1}\left(\frac{\sqrt{\frac{5\pi^2}{48}+\frac{22}{27}}}{2}\right) \tag{35}$$

Similarly, θ_{max} can be calculated for any value of γ and φ_2. Once the peak angle is determined, the limit of X_2 can be estimated by the condition $i_{DS,cont}(\theta_{max}) \le I_{max}$ for different value of γ and φ_2. For example, the limits of X_2 for three different conditions are derived as follows

$$|X_2(\gamma=0,\varphi_2=0)| \ge 2.93\times\frac{V_{DD}-V_K}{\mathrm{I}_{max}} \tag{36a}$$

$$|X_2(\gamma=0.5,\varphi_2=0)| \ge 1.77\times\frac{V_{DD}-V_K}{\mathrm{I}_{max}} \tag{36b}$$

$$|X_2(\gamma=0.5,\varphi_2=\pi)| \ge 2.65\times\frac{V_{DD}-V_K}{\mathrm{I}_{max}} \tag{36c}$$

The drain current waveforms for the limiting value of $X_2 = X_{2,lim}$ as defined in (36) are shown in Fig. 8. The maximum drain current reaches I_{max} at the limiting value of X_2. The variation of drain efficiency and output power in a continuous-mode of operation is shown in Fig. 9. Similar to inverse Class F PA, the efficiency performance remains almost constant with input nonlinearity compared to a Class B PA. Such behaviour allows second harmonic source termination other than a short circuit while maintains the PA efficiency performance.

C. Impact of Dynamic Knee Voltage in Continuous Inverse Class F Operation

So far, the analyses are carried out considering constant knee voltage. In reality, the device knee voltage shows a dynamic behaviour [40] with maximum device drain current. Thus, the knee voltage changes and demonstrate a dynamic behavior during the continuous inverse Class F operation due to current peaking [38]. The device knee voltage can be represented as

$$V_K = i_{DS,cont}(\max).\mathrm{R_{ON}} \tag{37}$$

where, $i_{ds,cont}(max)$ is the maximum drain current and R_{ON} is the ON resistance of the device which is mainly dependent on the mobility of the charge carriers and considered to be constant. Since the effective knee voltage of the device is increased due to current peaking of continuous inverse Class F operation, the efficiency is degraded, which is quantitatively estimated and validated with load pull measurements in [38]. However, to get a complete understanding of continuous inverse Class F PA performance, it is also important to consider the impact of dynamic knee voltage under input nonlinearity.

To compare PA performance quantitatively with and without input nonlinearity under dynamic knee voltage effect, an efficiency degradation factor (EDF) can be defined as

$$EDF(\%) = 100\times\frac{\eta(\gamma=0,\mathrm{X}_2=\infty)-\eta(\gamma,\varphi_2,\beta,\mathrm{X}_2)}{\eta(\gamma=0,\mathrm{X}_2=\infty)} \tag{38}$$

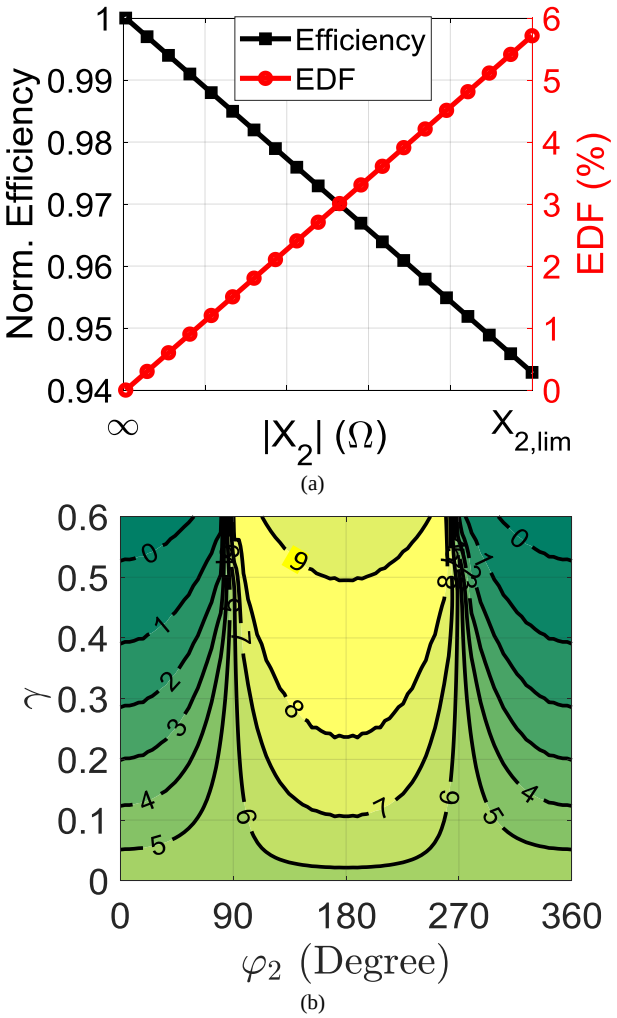

Fig. 10. (a) Variation of efficiency and efficiency degradation factor (*EDF*) without input nonlinearity, and (b) Variation of EDF_{max} with input nonlinearity in continuous mode inverse Class F operation.

where, X_2 is the second harmonic load reactance termination as considered in Section II(B). It is worth noting here that the efficiency (η) in (38) is related to dynamic knee voltage by (24) and (37). Thus, for an inverse Class F operation ($Z_{2L} = jX_2 = \infty$) without input nonlinearity, *EDF* turns out to be 0. The variation of efficiency and EDF without input nonlinearity (γ = 0) of a continuous inverse Class F PA is shown in Fig. 10(a) when X_2 is swept on the edge of the Smith chart up to the maximum allowable limit (causes $i_{ds,cont}(max) = I_{max}$). The efficiency is normalized by η (γ = 0, $X_2 = \infty$). It can be seen that the EDF reaches up to ~6% due to the increased and dynamic behaviour of the knee voltage.

With input nonlinearity, $i_{ds,cont}(max)$ can be calculated as a function of X_2 at different values of γ and φ_2. Thus, different sets of *EDF* at different levels of γ and φ_2 can be estimated. However, the maximum EDF is the figure of merit, happens when current reaches to I_{max} due to current peaking in continuous-mode operation and can be defined as

$$EDF_{\max}(\%) = 100\times\frac{\eta(\gamma=0,\mathrm{X}_2=\infty)-\eta(\gamma,\varphi_2,\beta,\mathrm{X}_2=\mathrm{X}_{2,\mathrm{lim}})}{\eta(\gamma=0,\mathrm{X}_2=\infty)} \tag{39}$$

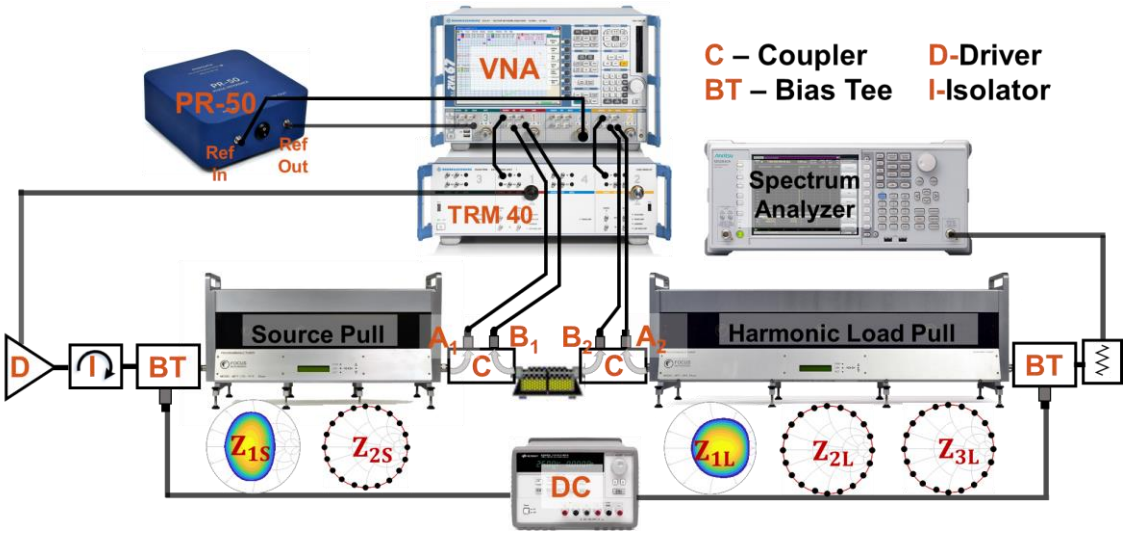

Fig. 11. Pulsed vector load pull measurement setup.

The EDF_{max} quantifies the efficiency variation of continuous inverse Class F PA with input nonlinearity and dynamic knee voltage compared to the ideal case with second harmonic source as a short termination and no dynamic knee voltage behavior. The variation of EDF_{max} in continuous inverse Class F operation under dynamic knee voltage and input nonlinearity is shown in Fig. 10(b). With the combined effect of dynamic knee voltage and input nonlinearity, the EDF_{max} can be as high as ~10%. On the other hand, the EDF_{max} can also be reduced by exploiting the input nonlinearity. In fact, there is a wide range of γ and φ_2 available for which reduced EDF_{max} can be achieved. Thus, the efficiency degradation by dynamic knee voltage behaviour due to current peaking in continuous inverse Class F PA can be recovered by carefully exploiting the input nonlinearity. Based on these analyses, efficient continuous inverse Class F PA is designed in this work utilizing input nonlinearity. Such approach opens up flexible source second harmonic design space compared to the fixed short circuit condition in traditional continuous inverse Class F PA designs.

III. Load Pull Measurements and Validation

A. Vector Load Pull Measurement Setup

In this work, vector load pull (VLP) measurements are performed to validate the theoretical analyses presented. VLP measurement provides useful information about device input characteristics which enhances measurement accuracy. The VLP measurement setup is shown in Fig. 11. The setup mainly consists of a load tuner MPT 1808, a source tuner MPT Lite 1808 and a phase reference unit Mesuro PR-50 from Focus Microwaves Group, VNA ZVA67 and its extension unit ZVAX-TRM40 from Rohde & Schwarz, a spectrum analyzer MS2840A from Anritsu, and DC power supplies E3634A from Agilent. The load tuner can tune the fundamental (Z_{1L}), second (Z_{2L}) and third (Z_{3L}) harmonic loads from 0.8 GHz to 1.8 GHz. The source tuner does the same for fundamental (Z_{1S}) and second (Z_{2S}) harmonic source impedances. To communicate, control and for synchronized measurements, Focus Device Characterization Suite (FDCS) [41] software is used. The setup mainly consists of two calibration steps. Firstly, tuner calibration and then wave calibration. The tuners are calibrated with the FDCS software using VNA ZVA67. For wave calibration, Mesuro calibration software is used along with the Mesuro phase reference unit PR-50 and a power meter NRP2 with power sensor NRP Z57 from Rohde & Schwarz. For wave measurements, both wave power and phase calibration are performed by Mesuro calibration software for A_1, B_1, A_2, B_2 as shown in Fig. 11 and utilized in the FDCS wave load-pull measurement software.

For inverse Class F PA, device compression level plays a vital role in performance metrics number. Thus, an inverse Class F PA is most often evaluated at constant compression level ensured by power sweep measurement at every load point. If continuous wave power sweeps are performed in such repetitive fashion for load pull measurements, GaN device performance are degraded due to thermal effect. To alleviate device heating and to avoid temperature effect, a pulsed wave load-pull measurement system is facilitated with a pulse modulator comes with the ZVAX-TRM40 extension unit. Such pulsed VLP measurement ensures accurate and repeatable measurements in a quasi-isothermal environment.

B. Load Pull Measurements and Validation

To validate the theoretical framework presented in the previous section, pulsed VLP measurements are performed with a Cree GaN device, CG2H40010F, at 1 GHz. However, to perform accurate load pull measurements and to probe intrinsic parameters, package and device parasitics, especially the drain to source capacitance (C_{DS}) is needed to be extracted accurately. To do so, efficiency minima phenomenon presented in [42], [43] is utilized. Thus, the device parasitic networks along with the package parameters are extracted as shown in Fig. 12(a). A fundamental load pull measurement with inverse Class F harmonic termination as shown in Fig. 12(b) is performed at the current generator plane by de-embedding the parasitic network. A fundamental load with maximum efficiency very close to the real axis on the Smith chart as shown in Fig. 12(b) ensures the accuracy of the parasitic parameter extraction. The reason why the second and third harmonic load terminations (Z_{2L} and Z_{3L})

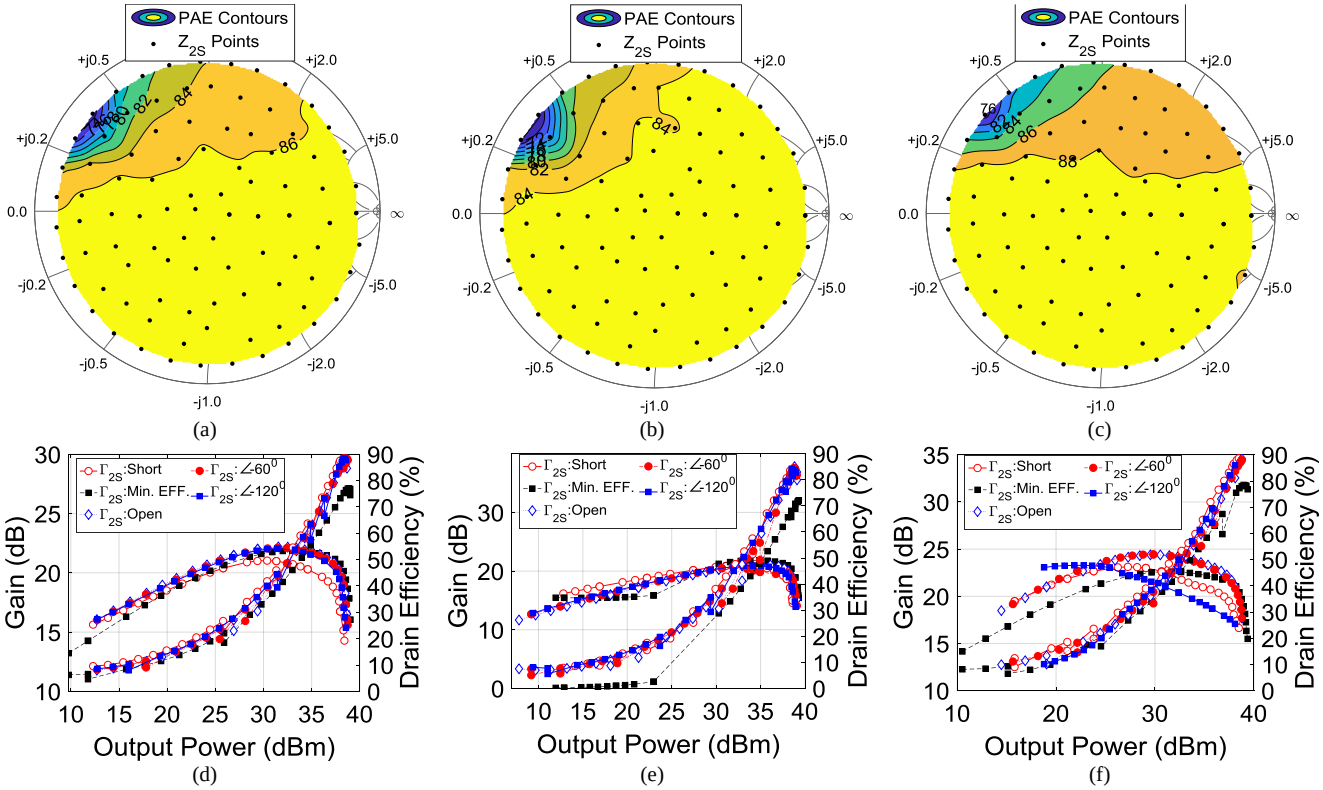

Fig. 13. Second harmonic source pull and power sweeps for different second harmonic load termination in continuous inverse Class F operation at (a, d) $Z_{2L} = \infty$, (b, e) Z_{2L} = +j120 Ω, and (c, f) Z_{2L} = -j120 Ω.

are not at the perfect open and short circuit is mainly due to the loss of the coupler, fixture, and the device parasitic network.

Once the parasitic information is extracted accurately, the impact of second harmonic source pull is investigated at different fundamental and harmonic loading conditions of continuous inverse Class F operation. This is accomplished in three steps:

1. Terminate second harmonic source (Z_{2S} or Γ_{2S}) to short and do a fundamental load pull for different harmonic terminations of continuous inverse Class F operation. Find the maximum efficiency points.
2. Terminate fundamental load at the maximum efficiency point found in step 1 and maintain corresponding harmonic terminations.
3. Perform second harmonic source pull.

Three-second harmonic source pull results with $Z_{2L} = \infty$, Z_{2L} = +j120 Ω, and Z_{2L} = -j120 Ω are shown in Fig. 13(a-c), respectively. In all cases, the contour plots in Fig. 13(a-c) clearly shows that there are certain regions where efficiency degrades about 10-15% which is predicted to be ~10% theoretically in Section-IIC by EDF_{max}. However, except that worst region where efficiency degrades, there is a wide range of second harmonic source terminations that show optimum efficiency performance of the device. This is unlikely to the fixed short circuit termination (Z_{2S}) in conventional PA designs and can be exploited to alleviate input MN design complexities in broadband operation. However, this observation goes in line with the theoretical prediction made in Section II(A-C). The power sweep results up to constant 5 dB gain compression for different Z_{2S} points including the one provides minimum efficiency are shown in Fig. 13(d-f). As expected, the efficiency remains almost constant except the minimum efficiency point.

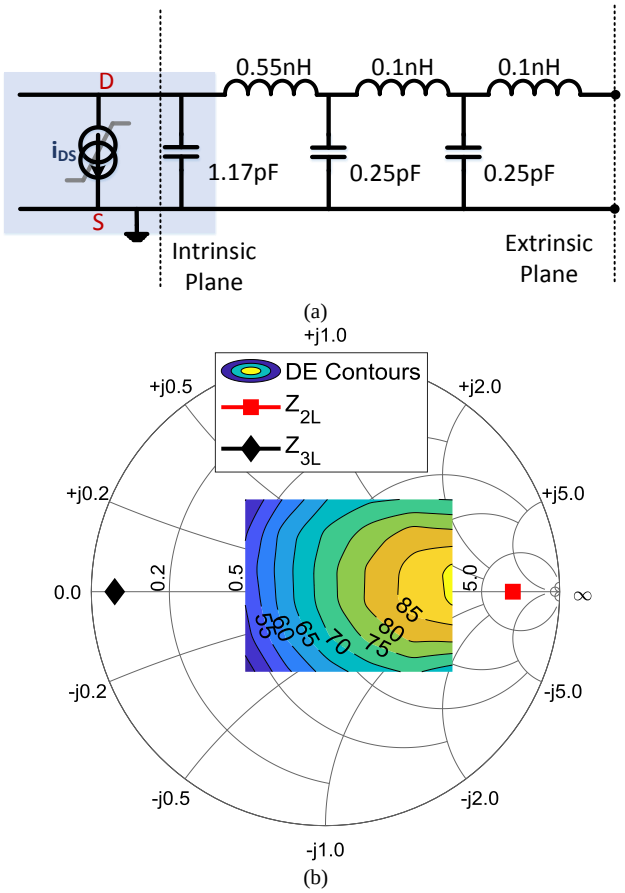

Fig. 12. (a) Device parasitic network, and (b) fundamental load pull at the current generator plane with inverse Class F termination.

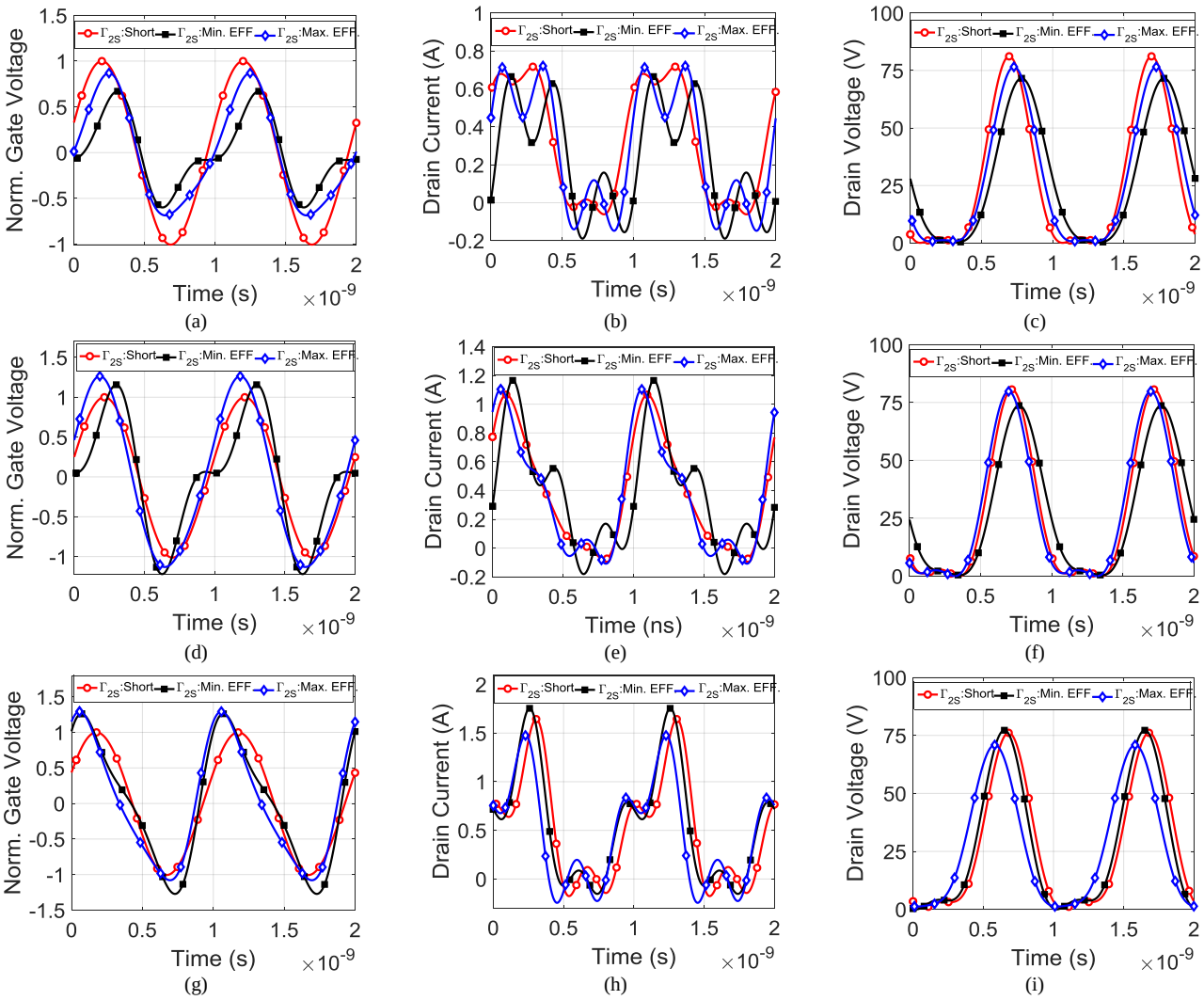

Fig. 14. Gate voltage, drain current and drain voltage waveforms for different second harmonic load termination in continuous inverse Class F operation at (a, b, c) $Z_{2L} = \infty$, (d, e, f) Z_{2L} = +j120 Ω, and (g, h, i) Z_{2L} = -j120 Ω.

To investigate the impact of input nonlinearity, the input gate voltage waveforms, output drain current, and voltage waveforms are probed and closely inspected at constant 3 dB gain compression level. The waveforms are presented in Fig. 14 for different second harmonic load terminations. For inverse Class F operation, $Z_{2L} = \infty$, the source second harmonic short termination generates sinusoidal gate voltage as shown in Fig. 14(a) as expected since $\gamma = 0$. However, at other Z_{2S} terminations, gate voltage waveforms deteriorate from the pure sinusoidal shape. However, the impact of input nonlinearity on the device efficiency performance depends on the combination of γ and φ_2 values as discussed in Section II. At the point of minimum efficiency, the input nonlinearity factor, γ, and the phase difference, φ_2, are found to be about 0.45 and 210°. The shape of the gate voltage waveforms matches well to the one derived in Fig. 2(d). Since the input nonlinearity factor is high, the EDF_{max} goes high too for a φ_2 value in the range of 90° to 270° as predicted in Fig. 10(b) and causes efficiency degradation. Also, the drain current peak remains almost constant as predicted in Fig. 5 since the phase difference φ_2 falls in the region of 90° to 270°. The drain voltage for all the Z_{2S} terminations remains half sinusoidal as in inverse Class F operation. The input gate voltage waveform shown in Fig. 14(d) is shaped in similar fashion for Z_{2L} = +j120 Ω due to the high value of γ about 0.65 and φ_2 in the range of 180° to 270° at the minimum efficiency Z_{2S} termination. For reactive Z_{2L} termination, drain current peaks left as expected. On the other hand, the input nonlinearity factor, γ, and the phase difference, φ_2 are found to be about 0.55 and 155° at the minimum efficiency Z_{2S} termination for Z_{2L} = -j120 Ω. The gate voltage waveforms are shown in Fig. 14(g). The current peaks to the right and the drain voltage waveforms remains half sinusoidal as shown in Fig. 14(h,i) for negative reactance of Z_{2L} termination as expected. These results validate the theoretical analyses conducted in Section II to estimate the large signal time domain waveforms and performance variation under input-output nonlinearity in continuous inverse Class F PA operation. Most importantly, it has been observed and confirmed that there are wide ranges of Z_{2S} terminations other than a short circuit possible which can maintain PA efficiency performance under input nonlinearity and dynamic knee behaviour of a practical device in continuous inverse Class F operation.

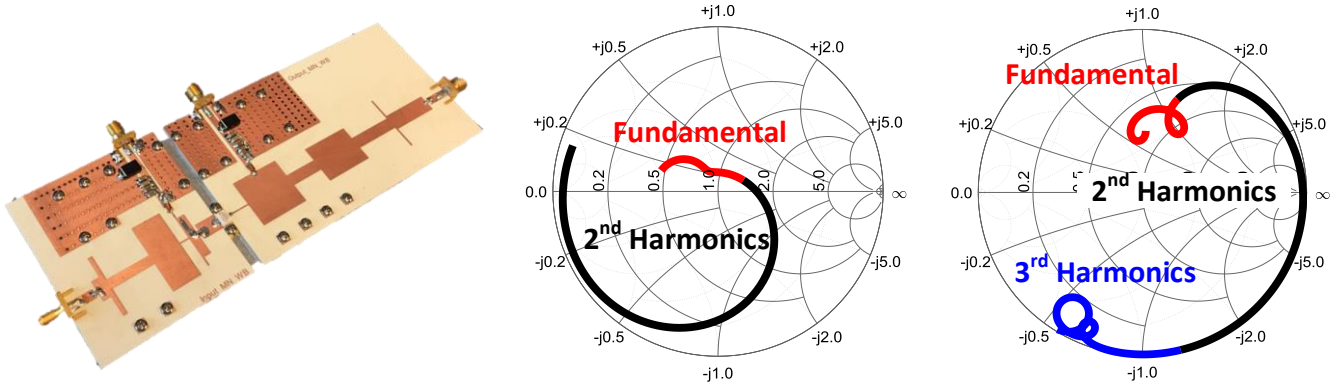

(a) (b) (c)

Fig. 15. (a) Fabricated PA prototype, (b) intrinsic trajectory of the source MN, (c) intrinsic trajectory of the load MN.

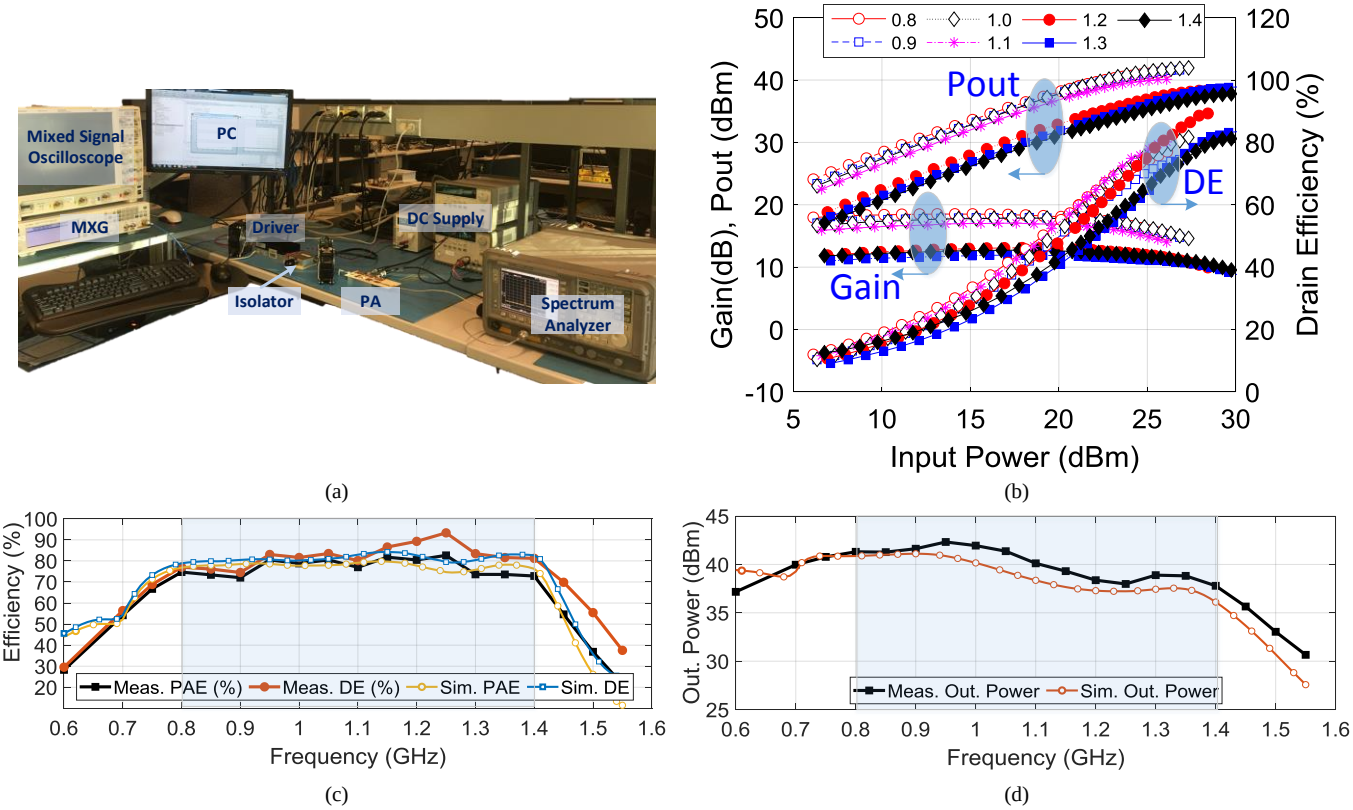

(a) (b) (c) (d)

Fig. 16. (a) PA measurement setup for CW and modulated signals, (b) measured power sweep over the band of operation, (c) measured and simulated efficiency at constant 3 dB gain compression, and (d) measured and simulated output power at constant 3 dB gain compression.

IV. PA Design and Measurement Results

The theoretical framework and the validation with VLP measurements presented in the previous sections open a new design space for high-efficiency continuous inverse Class F PAs exploiting input nonlinearity by second harmonic source terminations other than the short. The PA design steps with input non-linearity remains same as a traditional continuous inverse Class F but with an additional harmonic source pull to select flexible clockwise Z_{2S} terminations. This eliminates the complexities in realizing fixed short termination for broadband operation. To deploy the presented theoretical analyses, a broadband PA is designed with a Cree CG2H40010F GaN HEMT device. The fabricated prototype is shown in Fig. 15(a). The PA is designed for the operating frequency of 0.8-1.4 GHz. The intrinsic trajectories of the source and load MN are shown in Fig. 15(b) and Fig. 15(c), respectively. The second harmonic source terminations are placed in the optimum regions as shown in Fig 13(a-c) instead of a fixed short circuit. This not only helps to maintain efficiency performance of a continuous inverse Class F PA under input-output nonlinearity and dynamic knee voltage characteristics, also reduces complexities in input MN design. A fixed second harmonic short circuit condition is no more needed.

The setup for the PA measurement is shown in Fig. 16(a). The same setup is used for both continuous and modulated signal measurements. The setup consists of a driver, isolator, a signal generator MXG N5182A from Agilent Technologies to

TABLE I
PERFORMANCE COMPARISON WITH STATE-OF-THE-ART HIGH EFFICIENCY CONTINUOUS-MODE PAS

Ref	F (GHz)	FB (%)	P_{out} (dBm)	DE (%)	Class	Year
[12]	1.4-2.6	60	39.5-40.6	60-70	J	2009
[15]	1.45-2.45	51	40.4-42.3	70-81	CCF	2012
[21]	0.70-1.25	56	39-42	75-85	CCF	2013
[19]	0.50-0.90	57	40-41	75-84	2HT	2016
[24]	1.3-2.4	59	40.1-41.2	63-72	J	2017
[25]	0.5-0.95	62	38-40	73-79	$ECCF^{-1}$	2017
[26]	0.5-2.3	128	39.2-41.2	60-81	ECCF	2018
[27]	1.24-2.42	64	37-39.9	70-86	X	2018
This Work	0.8-1.4	55	38-42.3	75-93	$ICCF^{-1}$	2019

F: frequency, FB: fractional bandwidth, P_{out}: output power, DE: drain efficiency, CCF: continuous class F, 2HT: second harmonic tuned, ECCF: Extended continuous Class F, $ECCF^{-1}$: Extended continuous inverse Class F, $ICCF^{-1}$: Input controlled continuous inverse Class F.

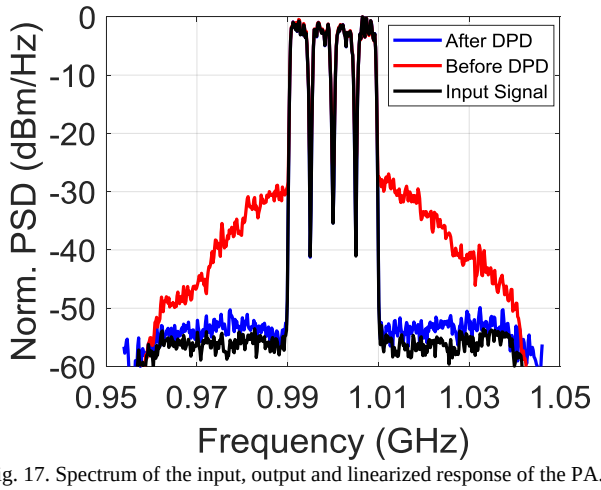

Fig. 17. Spectrum of the input, output and linearized response of the PA.

generate the both continuous and modulated input excitation, a vector signal analyzer 89600 VSA along with Infiniium MS09404A Mixed Signal Oscilloscope to record time domain response, and a spectrum analyzer Agilent E4405B which is used to capture continuous wave (CW) response of the PA. For accurate and repeatable measurements, an in-house automated CW measurement software is used.

The CW measurements are performed from 0.6-1.55 GHz. The transistor is biased in deep Class AB with V_{DS} = 28 V and quiescent current of I_{DS} = 20 mA. The power sweep results at different frequency points are shown in Fig. 16(b). The power added efficiency (PAE), drain efficiency (DE), and output power at constant 3 dB gain compression level are shown in Fig. 16(c) and Fig. 16(d), respectively, along with the simulated results. From the measurement results, it can be seen that PAE and DE are achieved more than 73% and 75%, respectively, over the frequency range 0.8-1.4 GHz. The feasible bandwidth of the PA with 70% DE is 0.75-1.45 GHz, which provides 64% fractional bandwidth. The measured output power of the PA is achieved more than 38 dBm over the band of operation. The performances of this work are summarized in Table 1 along with the state-of-the-art continuous-mode PA designs.

To assess the linearity performance of the PA, modulated signal measurements are performed with a 20 MHz, four carrier WCDMA signal centered at 1 GHz with a sampling rate of 92.16 MHz and with a peak to average power ratio (PAPR) of 11.25 dB. The input and output spectrum of the PA is shown in Fig. 17. The adjacent channel power ratio (ACPR) of the output spectrum of the PA is about -27.3 dBc and -28.1 dBc for the upper and lower adjacent channels, respectively. The output of the PA is modeled and linearized by digital predistortion (DPD) with a memory polynomial model having nonlinearity order of 7 and memory depth of 5. The linearized output spectrum is shown in Fig. 17. The ACPR of the linearized output spectrum is found to be -52.2 dBc and -52.4 dBc for the upper and lower adjacent channels, respectively.

V. CONCLUSIONS

This work presents a comprehensive analysis under the presence of input-output non-linearity and dynamic knee behavior of a practical FET device of a broadband inverse Class F PA design. Theoretical analysis shows new second harmonic source design space for continuous inverse Class F PA by exploiting input nonlinearity. This paper introduces a flexible source harmonic termination for broadband PA operation compared to a fixed short circuit termination in traditional continuous inverse Class F PAs. Thus, the proposed PA design space reduces input MN design complexities for broadband operation. The theoretical analyses are validated with VLP measurements and the application is demonstrated with a broadband PA design exhibiting high efficiency over a wide frequency range.

REFERENCES

[1] P. Colantonio, F. Giannini, and E. Limiti, *High Efficiency RF and Microwave Solid State Power Amplifiers*. John Wiley & Sons, 2009.

[2] F. H. Raab, "Class-F power amplifiers with maximally flat waveforms," *IEEE Trans. Microw. Theory Tech.*, vol. 45, no. 11, pp. 2007–2012, Nov. 1997.

[3] P. Colantonio, F. Giannini, G. Leuzzi, and E. Limiti, "Multiharmonic manipulation for highly efficient microwave power amplifiers," *Int. J. RF Microw. Comput.-Aided Eng.*, vol. 11, no. 6, pp. 366–384, Nov. 2001.

[4] F. H. Raab, "Maximum efficiency and output of class-F power amplifiers," *IEEE Trans. Microw. Theory Tech.*, vol. 49, no. 6, pp. 1162–1166, Jun. 2001.

[5] P. J. Tasker, "Practical waveform engineering," *IEEE Microw. Mag.*, vol. 10, no. 7, pp. 65–76, Dec. 2009.

[6] J. H. Kim, G. D. Jo, J. H. Oh, Y. H. Kim, K. C. Lee, and J. H. Jung, "Modeling and Design Methodology of High-Efficiency Class-F and Class-F^{-1} Power Amplifiers," *IEEE Trans. Microw. Theory Tech.*, vol. 59, no. 1, pp. 153–165, Jan. 2011.

[7] J. H. Kim, S. J. Lee, B. H. Park, S. H. Jang, J. H. Jung, and C. S. Park, "Analysis of High-Efficiency Power Amplifier Using Second Harmonic Manipulation: Inverse Class-F/J Amplifiers," *Ieee Trans. Microw. Theory Tech.*, vol. 59, no. 8, pp. 2024–2036, Aug. 2011.

[8] J. Moon, S. Jee, J. Kim, J. Kim, and B. Kim, "Behaviors of Class-F and Class-F^{-1} Amplifiers," *IEEE Trans. Microw. Theory Tech.*, vol. 60, no. 6, pp. 1937–1951, Jun. 2012.

[9] J. Moon, J. Kim, and B. Kim, "Investigation of a Class-J Power Amplifier with a Nonlinear Cout for Optimized Operation," *IEEE Trans. Microw. Theory Tech.*, vol. 58, no. 11, p. 12, Nov. 2010.

[10] P. Colantonio, F. Giannini, G. Leuzzi, and E. Limiti, "Theoretical facet and experimental results of harmonic tuned PAs," *Int. J. RF Microw. Comput.-Aided Eng.*, vol. 13, no. 6, pp. 459–472, Oct. 2003.

[11] S. C. Cripps, P. J. Tasker, A. L. Clarke, J. Lees, and J. Benedikt, "On the Continuity of High Efficiency Modes in Linear RF Power Amplifiers," *IEEE Microw. Wirel. Compon. Lett.*, vol. 19, no. 10, pp. 665–667, Oct. 2009.

[12] P. Wright, J. Lees, J. Benedikt, P. J. Tasker, and S. C. Cripps, "A Methodology for Realizing High Efficiency Class-J in a Linear and Broadband PA," *IEEE Trans. Microw. Theory Tech.*, vol. 57, no. 12, pp. 3196–3204, Dec. 2009.

[13] V. Carrubba *et al.*, "On the Extension of the Continuous Class-F Mode Power Amplifier," *IEEE Trans. Microw. Theory Tech.*, vol. 59, no. 5, pp. 1294–1303, May 2011.
[14] V. Carrubba *et al.*, "The Continuous Inverse Class-F Mode With Resistive Second-Harmonic Impedance," *IEEE Trans. Microw. Theory Tech.*, vol. 60, no. 6, pp. 1928–1936, Jun. 2012.
[15] N. Tuffy, L. Guan, A. Zhu, and T. J. Brazil, "A Simplified Broadband Design Methodology for Linearized High-Efficiency Continuous Class-F Power Amplifiers," *IEEE Trans. Microw. Theory Tech.*, vol. 60, no. 6, pp. 1952–1963, Jun. 2012.
[16] S. Rezaei, L. Belostotski, F. M. Ghannouchi, and P. Aflaki, "Integrated Design of a Class-J Power Amplifier," *IEEE Trans. Microw. Theory Tech.*, vol. 61, no. 4, pp. 1639–1648, Apr. 2013.
[17] S. Rezaei, L. Belostotski, M. Helaoui, and F. M. Ghannouchi, "Harmonically Tuned Continuous Class-C Operation Mode for Power Amplifier Applications," *IEEE Trans. Microw. Theory Tech.*, vol. 62, no. 12, pp. 3017–3027, Dec. 2014.
[18] M. Sakalas, S. Preis, D. Gruner, and G. Boeck, "Iterative design of a harmonically tuned multi-octave broadband power amplifier," in *2014 IEEE MTT-S International Microwave Symposium (IMS2014)*, pp. 1–4, 2014.
[19] T. Sharma, R. Darraji, and F. Ghannouchi, "A Methodology for Implementation of High-Efficiency Broadband Power Amplifiers With Second-Harmonic Manipulation," *IEEE Trans. Circuits Syst. II Express Briefs*, vol. 63, no. 1, pp. 54–58, Jan. 2016.
[20] T. Sharma, R. Darraji, F. Ghannouchi, and N. Dawar, "Generalized Continuous Class-F Harmonic Tuned Power Amplifiers," *IEEE Microw. Wirel. Compon. Lett.*, vol. 26, no. 3, pp. 213–215, Mar. 2016.
[21] Z. Lu and W. Chen, "Resistive Second-Harmonic Impedance Continuous Class-F Power Amplifier With Over One Octave Bandwidth for Cognitive Radios," *IEEE J. Emerg. Sel. Top. Circuits Syst.*, vol. 3, no. 4, pp. 489–497, Dec. 2013.
[22] T. Sharma, R. Darraji, P. Mousavi, and F. m. Ghannouchi, "Generalized design of continuous-mode second harmonic tuned amplifiers," *Microw. Opt. Technol. Lett.*, vol. 58, no. 12, pp. 2787–2789, Dec. 2016.
[23] M. Yang, J. Xia, Y. Guo, and A. Zhu, "Highly Efficient Broadband Continuous Inverse Class-F Power Amplifier Design Using Modified Elliptic Low-Pass Filtering Matching Network," *IEEE Trans. Microw. Theory Tech.*, vol. 64, no. 5, pp. 1515–1525, May 2016.
[24] S. Saxena, K. Rawat, and P. Roblin, "Continuous Class-B/J Power Amplifier Using Nonlinear Embedding Technique," *IEEE Trans. Circuits Syst. II Express Briefs*, vol. PP, no. 99, pp. 1–1, 2016.
[25] Y. Dong, L. Mao, and S. Xie, "Extended Continuous Inverse Class-F Power Amplifiers With Class-AB Bias Conditions," *IEEE Microw. Wirel. Compon. Lett.*, vol. 27, no. 4, pp. 368–370, Apr. 2017.
[26] S. Y. Zheng, Z. W. Liu, X. Y. Zhang, X. Y. Zhou, and W. S. Chan, "Design of Ultrawideband High-Efficiency Extended Continuous Class-F Power Amplifier," *IEEE Trans. Ind. Electron.*, vol. 65, no. 6, pp. 4661–4669, Jun. 2018.
[27] X. Li, M. Helaoui, and X. Du, "Class-X–Harmonically Tuned Power Amplifiers With Maximally Flat Waveforms Suitable for Over One-Octave Bandwidth Designs," *IEEE Trans. Microw. Theory Tech.*, vol. PP, no. 99, pp. 1–12, 2018.
[28] C. Friesicke, R. Quay, and A. F. Jacob, "The Resistive-Reactive Class-J Power Amplifier Mode," *IEEE Microw. Wirel. Compon. Lett.*, vol. 25, no. 10, pp. 666–668, Oct. 2015.
[29] Z. Dai, S. He, J. Pang, J. Peng, C. Huang, and F. You, "Sub-optimal matching method for dual-band class-J power amplifier using real frequency technique," *Antennas Propag. IET Microw.*, vol. 11, no. 9, pp. 1218–1226, 2017.
[30] P. Colantonio, F. Giannini, G. Leuzzi, and E. Limiti, "High efficiency low-voltage power amplifier design by second-harmonic manipulation," *Int. J. RF Microw. Comput.-Aided Eng.*, vol. 10, no. 1, pp. 19–32, Dec. 1999.
[31] T. Sharma, S. Shukla, D. G. Holmes, R. Darraji, J. K. Jones, and F. Ghannouchi, "Input Harmonic Sensitivity in High-Efficiency GaN Power Amplifiers," in *2018 IEEE/MTT-S International Microwave Symposium - IMS*, pp. 461–464, 2018.
[32] P. M. White, "Effect of input harmonic terminations on high efficiency class-B and class-F operation of PHEMT devices," in *1998 IEEE MTT-S International Microwave Symposium Digest (Cat. No.98CH36192)*, 1998, vol. 3, pp. 1611–1614 vol.3.
[33] T. Canning, P. Tasker, and S. Cripps, "Waveform Evidence of Gate Harmonic Short Circuit Benefits for High Efficiency X-Band Power Amplifiers," *IEEE Microw. Wirel. Compon. Lett.*, vol. 23, no. 8, pp. 439–441, Aug. 2013.
[34] K.-I. Jeon, Y.-S. Kwon, and S.-C. Hong, "Input harmonics control using non-linear capacitor in GaAs FET power amplifier," in *Microwave Symposium Digest, 1997., IEEE MTT-S International*, 1997, vol. 2, pp. 817–820, 1997.
[35] M. Haynes, S. C. Cripps, J. Benedikt, and P. J. Tasker, "PAE improvement using 2nd harmonic source injection at x-band," in *2012 Workshop on Integrated Nonlinear Microwave and Millimetre-wave Circuits*, pp. 1–3, 2012.
[36] G. Bosi, A. Raffo, G. Vannini, E. Cipriani, P. Colantonio, and F. Giannini, "Gate waveform effects on high-efficiency PA design: An experimental validation," in *2014 9th European Microwave Integrated Circuit Conference*, pp. 329–332, 2014.
[37] A. Alizadeh and A. Medi, "Investigation of a Class-J Mode Power Amplifier in Presence of a Second-Harmonic Voltage at the Gate Node of the Transistor," *Ieee Trans. Microw. Theory Tech.*, vol. 65, no. 8, pp. 3024–3033, Aug. 2017.
[38] S. K. Dhar, T. Sharma, R. Darraji, M. Helaoui, and F. M. Ghannouchi, "On the Continuity of Continuous Inverse Class F Power Amplifiers," in *IEEE MTT-S Latin America Microwave Conference*, pp. 1–3, 2018.
[39] T. Sharma *et al.*, "High-Efficiency Input and Output Harmonically Engineered Power Amplifiers," *IEEE Trans. Microw. Theory Tech.*, vol. PP, no. 99, pp. 1–13, 2017.
[40] J. C. Pedro, L. C. Nunes, and P. M. Cabral, "A Simple Method to Estimate the Output Power and Efficiency Load-Pull Contours of Class-B Power Amplifiers," *IEEE Trans. Microw. Theory Tech.*, vol. 63, no. 4, pp. 1239–1249, Apr. 2015.
[41] "Focus Device Characterization Suite (FDCS)." [Online]. Available: https://focus-microwaves.com/fdcs/.
[42] T. Sharma *et al.*, "Simplified First-Pass Design of High-Efficiency Class-F^{-1} Power Amplifiers Based on Second-Harmonic Minima," *IEEE Trans. Microw. Theory Tech.*, pp. 1–15, 2019.
[43] T. Sharma *et al.*, "On the Second-Harmonic Null in Design Space of Power Amplifiers," *IEEE Microw. Wirel. Compon. Lett.*, pp. 1–3, 2018.

Sagar K. Dhar (S'11) is currently pursuing the Ph.D. degree at the iRadio Lab, University of Calgary, Calgary, AB, Canada. He has authored or co-authored over 20 publications and holds 3 U.S. patents. His current research interests include high-efficiency RF power amplifiers, MMIC active and passive RF circuits and systems, and load–pull techniques. Mr. Dhar was a recipient of the Izaak Walton Killam Pre-Doctoral Scholarship, the AITF Doctoral Scholarship, the Open Doctoral Scholarship, the Academic Excellence Award, and the Research Productivity Award.

Tushar Sharma (S'10) is a post-doctoral research associate at Princeton University, NJ, USA. He completed Ph.D. degree at the University of Calgary, Calgary, AB, Canada in 2018. In 2016 and 2017, he joined NXP Semiconductors, Chandler, AZ, USA, as a Research and Development RF engineer to work in field of gallium nitride technology evaluation and

design for 5G base station applications. Mr. Sharma is a recipient of the Izaak Walton Killam Pre-Doctoral Scholarship, Alberta Science and Innovation under 30 Future leader award, the AITF Doctoral Scholarship, the Alberta Transformative Talent scholarship, the Academic Excellence Award, and the Research Productivity Award. He has authored and coauthored over 20 refereed publications and 2 pending US patents. His current research interests include high-efficiency broadband RF/mmW power amplifiers, waveform engineering techniques, and active/passive load-pull techniques.

Ramzi Darraji (S'10, M'13) received the M.Sc. degree in communications engineering from the École Supérieure des Communications de Tunis, Ariana, Tunisia, in 2008 and the Ph.D. degree in electrical engineering from the University of Calgary, Calgary, AB, Canada, in 2013.

He is currently with Ericsson Canada Inc., Ottawa, ON, Canada. He has authored and co-authored over 40 refereed publications and 4 patents. His current research interests include advanced power amplifier design and RF front-end architectures for cellular base transceiver stations.

Damon G. Holmes (M' 13) received the B.Sc. and M.Sc. degrees from the University of Calgary, Calgary, AB, Canada, in 2002 and 2005, respectively. He has gained over 15 years of industrial experience with Nortel Networks Wireless Infrastructure Group, Freescale and NXP Semiconductors, Chandler, AZ, USA, where he is involved in transmitter architectures, advanced power amplifier design including Doherty, waveform shaping and large signal device modeling in support of cellular and wireless communication technology. He currently manages the New Technology Integration design efforts for high-power macro-cell applications at NXP Semiconductors' Radio Power Solutions business unit. He holds 23 patents, awarded and pending.

Suhas Illath Veetil received the M.Sc. degree in Electrical Engineering from the University of Calgary, Calgary, Canada in 2014 and the B.Tech. Degree in Electronics and Communication Engineering from Mahatma Gandhi University, India in 2008. He is currently an Application engineer at Focus Microwaves Group, Montreal, Canada. Prior to joining Focus Microwaves, he was a research associate with the Intelligent RF Radio Technology Laboratory (iRadio Lab), Department of Electrical and Computer Engineering, University of Calgary. His research interests include advanced load pull techniques for transistor characterization and RF system level design.

Vince Mallette is currently the Director of sales and business development at Focus Microwaves, Montreal, Canada. He has over 12 years of experience in international sales, marketing and strategic business development in Test and Measurement. His current interests include global strategic sales and marketing initiatives and expansion in new markets as well as continued expansion among existing clients.

Fadhel M. Ghannouchi (S'84–M'88–SM'93–F'07) is currently a Professor, Alberta Innovates/the Canada Research Chair, and the Founding Director of the iRadio Laboratory, Department of Electrical and Computer Engineering, University of Calgary, Calgary, AB, Canada. He held several invited positions at several academic and research institutions in Europe, North America, and Japan. He has provided consulting services to a number of microwave and wireless communications companies. He has authored or co-authored over 650 publications. He holds 16 U.S. patents with 4 pending. His current research interests include microwave instrumentation and measurements, nonlinear modeling of microwave devices and communications systems, design of power- and spectrum-efficient microwave amplification systems, and design of intelligent RF transceivers for wireless and satellite communications.